Role of Hydrothermal Reaction Time on Defect-and Strain-Engineered Few-Layered MoS_2 Nanoflowers for Tunable Band Gap and Enhanced Visible-Light Photocatalysis

Bhagyalakshmi Balan,[a] Minu Elizabeth Thomas,[a] Treesa K. James[a] and Suresh Mathew[a*]

a. School of Chemical Sciences, Mahatma Gandhi University, Kottayam, Kerala – 686 560, India

E-mail: bhagyalakshmi.udaya@gmail.com, sureshmathewmgu@gmail.com

Supporting Information

Text S1. Materials used

Ammonium heptamolybdate tetrahydrate ($(NH_4)_6Mo_7O_{24}.4H_2O$), and methylene blue (MB) were obtained from Merck Specialities Pvt. Ltd and thiourea (CH_4N_2S) from Himedia Chemicals. Carbon black, poly(vinylidene fluoride) (PVDF), N-methyl pyrrolidone (NMP), ciprofloxacin (CIP) and tetracycline (TC) from Sigma Aldrich. All the reagents used in the synthesis were analytically pure and used without further purification.

Text S2. Materials characterization

FT-IR spectra were used to identify the functional groups in MoS_2 samples, recorded on a PerkinElmer 400 Spectrometer in the 4000-400 cm^{-1} range. The crystal structures were studied using a Rigaku Mini Flex 600 powder X-ray diffractometer with monochromatic Cu Kα (λ = 0.154 nm) radiation. Raman spectra of the samples were obtained from a WITEC ALPHA300 RA - Confocal Raman Microscope with a 532 nm DPSS laser as the excitation laser. The morphology and microstructure of the samples were determined using an FE-SEM (MAIA3 XMH model microscope) and an HR-TEM (JEOL JEM-2100 microscope) instrument. The samples' chemical states and surface chemistry were investigated through XPS analysis (Omicron Nanotechnology XPS was equipped with a DR400 X-ray source). The UV-visible diffuse reflectance spectrum (UV-DRS) samples were obtained from a Shimadzu UV-2600 UV-visible spectrophotometer. Photoluminescence (PL) spectra were obtained using a PerkinElmer Fluorescence Spectrometer FL 8500. EPR analyses were carried out at room temperature using a Bruker EMX MICRO X spectrometer. The specific surface area was measured using Nova Touch L×2 by a Quantachrome analyzer.

Text S3. Electrochemical characterizations

The electrochemical activity of the samples was analyzed using a Biologic SP 200 electrochemical workstation using a three-electrode system. Platinum wire and Ag/AgCl are the counter and reference electrodes, respectively. For working electrode preparation, an 8:1:1 ratio of photocatalyst, carbon black, and PVDF in NMP was prepared and coated onto an FTO glass plate, approximately over an area of 1.0 × 1.0 cm^2. Then, the FTO glass sheet was dried

at 60°C for 6 hours. Electrochemical impedance spectroscopy (EIS) and Mott-Schottky (MS) analysis were studied in 0.5 M H_2SO_4. The applied potential is converted to the reversible hydrogen electrode (RHE) by Eq. 1.

$$V_{RHE} = V_{\frac{Ag}{AgCl}} + 0.059 \times pH + V^{0}_{Ag/AgCl} \qquad (1)$$

Where V_{RHE} denotes the converted potential vs. RHE, $V_{Ag/AgCl}$ is the measured potential w.r.t. the Ag/AgCl electrode, and $V^{0}_{Ag/AgCl} = 0.1976$ at 25^0C.

Text S4. Computational details

Density functional theory (DFT) calculations were performed using Gaussian 16.C.01.[1] to investigate the structural stability, electronic properties, and pollutant adsorption behavior of few-layer MoS_2. Cluster models representing 1-5 layers of MoS_2 were constructed by truncating the hexagonal 2H-MoS_2 lattice while preserving the local coordination geometry around Mo and S atoms. All structures were analyzed using the B3LYP-D3(BJ) functional to account for long-range dispersion interactions, which are essential for layered materials. The LANL2DZ effective core potential and basis set were applied to molybdenum atoms, while the 6-311+G(d,p) basis set was used for sulphur, oxygen, carbon, nitrogen, fluorine, and hydrogen atoms.

Cohesive energy was employed as it encapsulates the stability acquired when monolayers assemble into few-layer MoS_2, thereby directly reflecting the layer-dependent photocatalytic behavior, rather than formation energy, which pertains to elemental processes rather than interlayer interactions.[2] To quantify stacking stability, the cohesive energy per layer $(E_{coh}(n))$ for an n-layer cluster, the computation was performed using Eq. 2.

$$E_{coh}(n) = \frac{nE_1 - E_n}{n} \qquad (2)$$

where $E_1 \; and \; E_n$ are the total electronic energies of the monolayer and n-layer cluster, respectively.

The adsorption of TC and CIP on monolayer MoS_2 was evaluated by building antibiotic-MoS_2 composite models with the antibiotic molecules placed in their lowest-energy orientations above the MoS_2 basal plane. Adsorption energies were calculated by Eq.3.

$$E_{ads} = E_{MoS_2 + antibiotic} - \left(E_{MoS_2} + E_{antibiotic}\right) \qquad (3)$$

where negative values indicate favourable adsorption.

Molecular electrostatic potential (MESP) maps were generated to illustrate regions of electron richness and electron deficiency pertinent to photocatalytic reactivity. Frontier molecular orbital (FMO) energies, including the highest occupied molecular orbital (HOMO) and the lowest unoccupied molecular orbital LUMO, were derived from Gaussian output files to elucidate variations in the band gap with an increasing number of MoS_2 layers and to evaluate interfacial charge transfer between MoS_2 and dye molecules. All visualizations were produced utilizing GaussView 6.1.1.[3] Secondary non-covalent interactions (NCI) were examined using the Multiwfn program, with the corresponding isosurfaces rendered and visualized in Visual molecular dynamics (VMD).[4,5]

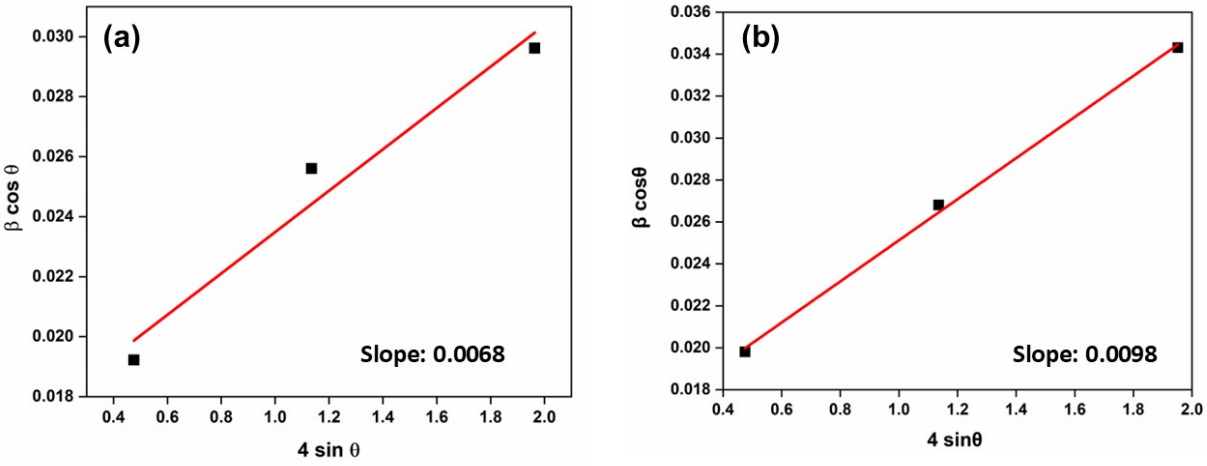

Fig. S1. W-H plots of MoS_2 samples.

Table S1: Calculation of strain in MoS_2 NFs				
Sample	**(hkl)**	**2θ**	**d_{hkl} (A°)**	**ε (no dimension)**
MoS_2-1	(002)	13.86	6.38	**0.0068**
	(100)	33.07	2.70	
	(110)	58.83	1.56	
MoS_2-2	(002)	13.77	6.42	**0.0098**
	(100)	33.39	2.68	
	(110)	58.53	1.57	

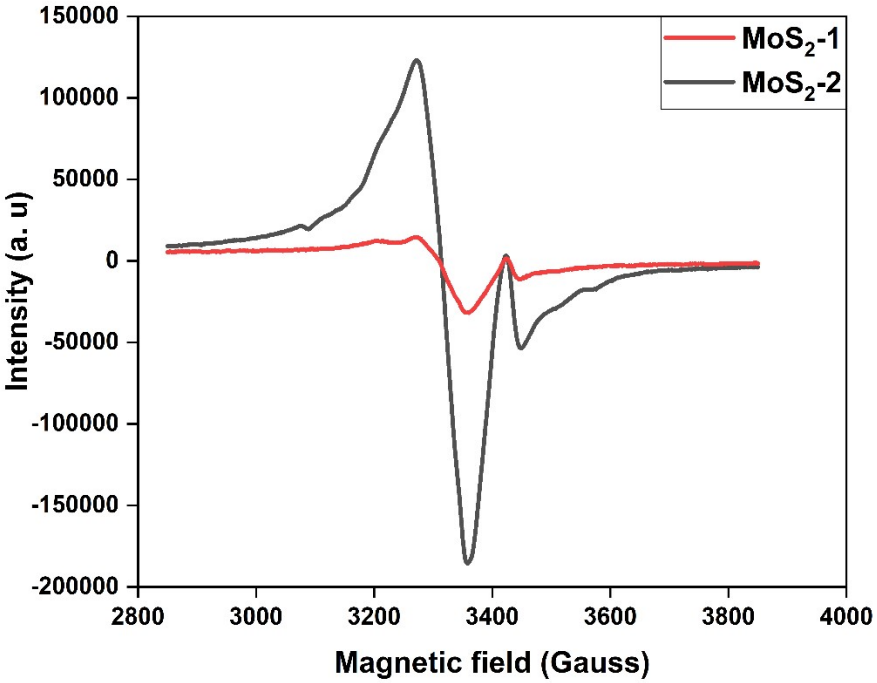

Fig. S2. EPR analysis of MoS_2 samples.

Table S2: ICP-OES analysis data			
Sample	**Mo**	**S**	**Mo:S Raio**
MoS_2-1	34.10	65.90	1:1.93
MoS_2-2	34.32	65.67	1:1.91

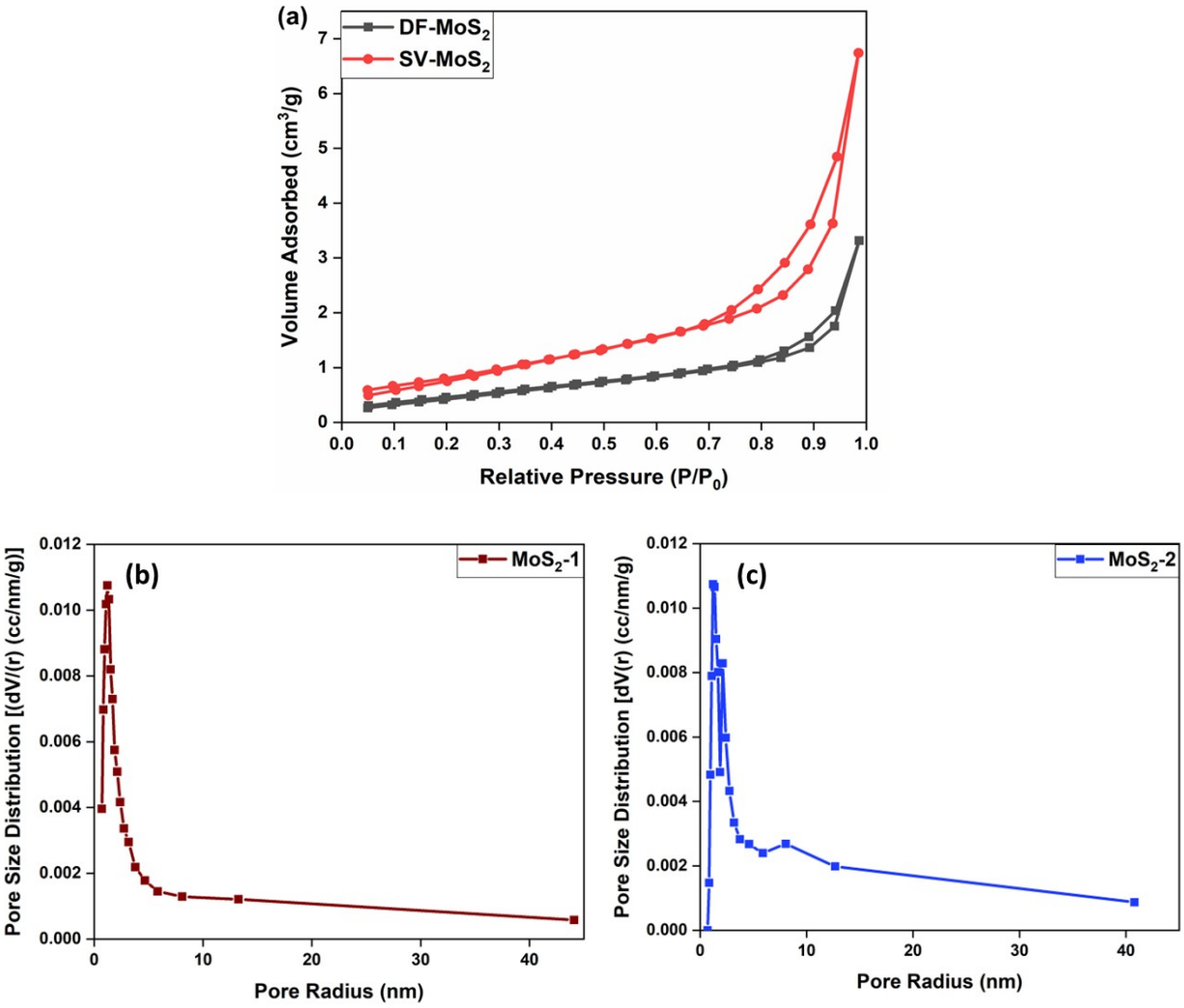

Fig. S3. (a) BET isotherm of MoS_2 samples; (b) Pore-size distribution curve of MoS_2 samples.

Table S3: Surface and porous parameters of the samples			
Sample	BET surface area (m^2/g)	Avg. pore radius (nm)	Avg. pore volume (cm^3/g)
MoS_2-1	20.95	5.98	0.062
MoS_2-2	25.47	6.85	0.087

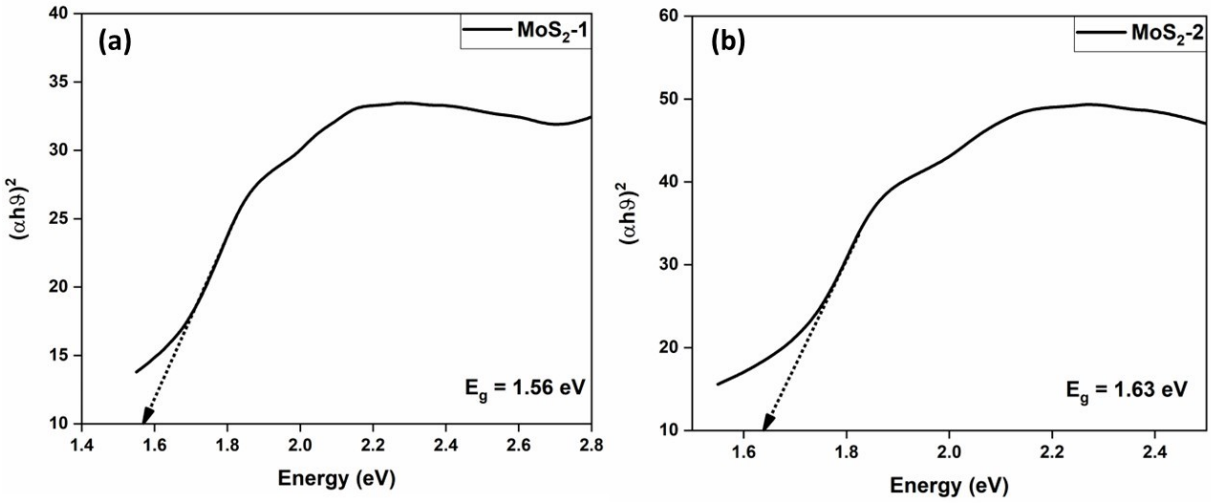

Fig. S4. Tauc plot of MoS_2 samples.

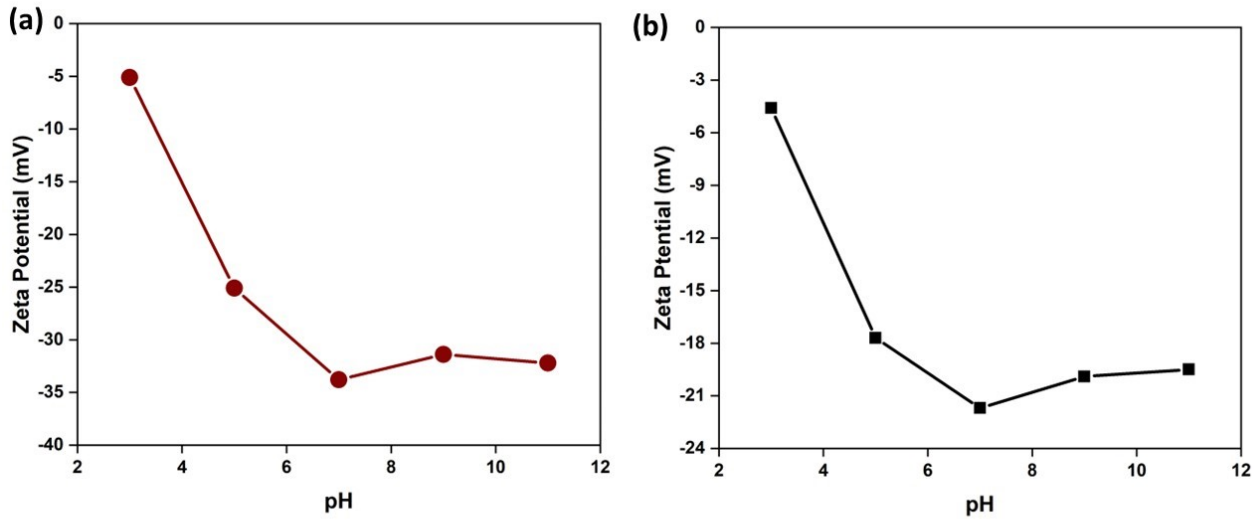

Fig. S5. Zeta potential of MoS_2-2 as a function of pH in the photocatalytic degradation of (a) TC and (b) CIP.

Table S4: Comparison of synthesized MoS_2 NFs with other catalysts								
Catalyst	Dye	Catalyst dosage (g/L)	Dye concentration (mg/L)	pH	Light source	Degradation Percentage (%)	Time taken for degradation (min)	Ref.
$NiCo_2O_4/ZnO$	MB	0.4	10	7	Visible lamp (400 W)	92.85	120	6
SnO_2@g-C_3N_4	MB	0.1	100	6	Sun light	97	45	7
$CoNi_2S_4/MoS_2$	MB	0.2	10	11	Visible light (250 W)	100	90	8
C-TiO_2-MoS_2	MB	0.2	100	11	Xenon lamp (3 W)	99.6	45	9
Bi_2WO_6-ZnO/GO	MB	1	20	3.04	Visible light	87.9	180	10
MoS_2/Co_3O_4	MB	0.4	10	-	Visible light (250 W)	99.5	120	11
Mn-doped rGO/NiO/g-C_3N_4	MB	1	10	11	UV lamp (85 W)	98.3	90	12
MoS_2 NFs	MB	0.2	10	6.5	Natural sunlight	98.46	75	This work
Mn_2O_3@GO-MoS_2	TC	0.1	50	6	Visible light (400 W)	98.91	15	13
MoS_2/Graphene aerogel	TC	0.5	5	7	Hg vapour lamp (250 W)	97	120	14
MoS_2/Graphene aerogel	TC	0.5	5	7	Hg lamp (250 W)	95	90	15
$MoS_2/CuBi_2O_4$	TC	0.6	5	5.3	Xenon lamp (100 W)	83	180	16
g-$C_3N_4/Fe_3O_4/In_2O_3/MoS_2$	TC	0.2	10	9	Xenon lamp (300 W)	94.1	240	17
Biochar silica@BiOCl	TC	0.2	10	11	Xenon lamp (300 W)	96.2	90	18
β-In_2S_3	TC	0.5	10	6.5	LED lamp (60 W)	85.5	240	19
MoS_2 NFs	TC	0.2	10	7	Natural sunlight	99	75	This work
$CuNb_{13}O_{33}$/g-C_3N_5	CIP	0.75	10	7	Tungsten halogen lamp (500 W)	98	120	20
CdS/CuO	CIP	0.5	10	5	Visible light	100	180	21
MoS_2/Bi_2WO_6	CIP	0.4	20	7	Xe lamp (300W)	99.6	60	22
C-dots/ZnO	CIP	0.6	12	6.3	Natural sunlight	98	110	23
$MgFe_2O_4$/UiO-67	CIP	0.25	10	8.02	LED lamps (300 W)	99.62	90	24
$Fe_2O_3/Fe_3O_4/Cr_2O_3$/rGO	CIP	0.6	10	7	Natural sunlight (Av. Intensity 730 W m^{-2})	92.1	120	25
$ZnMn_2O_4/V_2O_5$	CIP	0.4	20	6	Xenon lamp (300 W)	98.7	100	26
MoS_2 NFs	CIP	0.2	10	7	Natural sunlight	98.30	90	This work

Table S5: Parameters of tap water and river water used in the photocatalysis by MoS_2-2		
Parameters	Tap water	River water
pH	6.27	6.59
Na^+ (mg L^{-1})	5.56	1.62
K^+ (mg L^{-1})	1.44	0.46
Mg^{2+} (mg L^{-1})	4.76	2.38
Ca^{2+} (mg L^{-1})	3.92	3.92
SO_4^{2-} (mg L^{-1})	0.28	0.17
Cl^- (mg L^{-1})	0.29	0.16
NO_3^- (mg L^{-1})	0.18	0.17
F^- (mg L^{-1})	Not detected	Not detected
PO_4^{3-} (mg L^{-1})	Not detected	Not detected

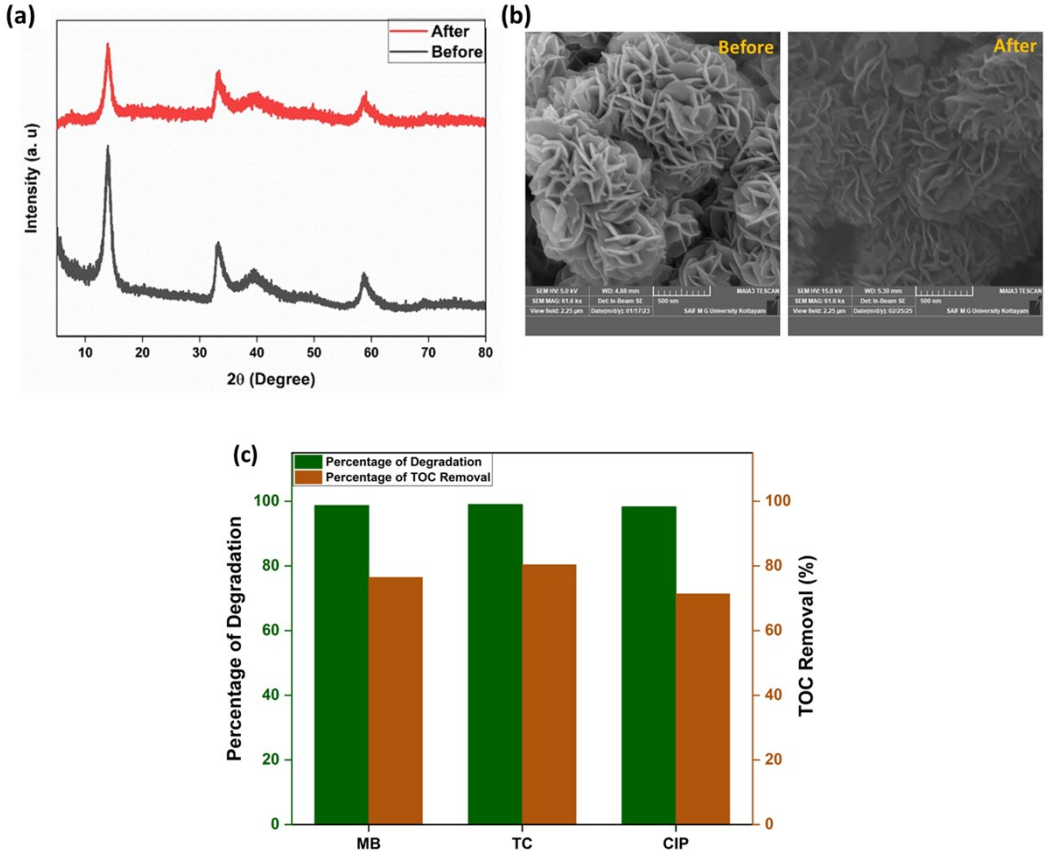

Fig. S6. Comparison of XRD (a) and FE-SEM images (b) of MoS_2-2 before and after degradation; (c) Percentage of degradation and TOC removal of MoS_2-2 in tap water.

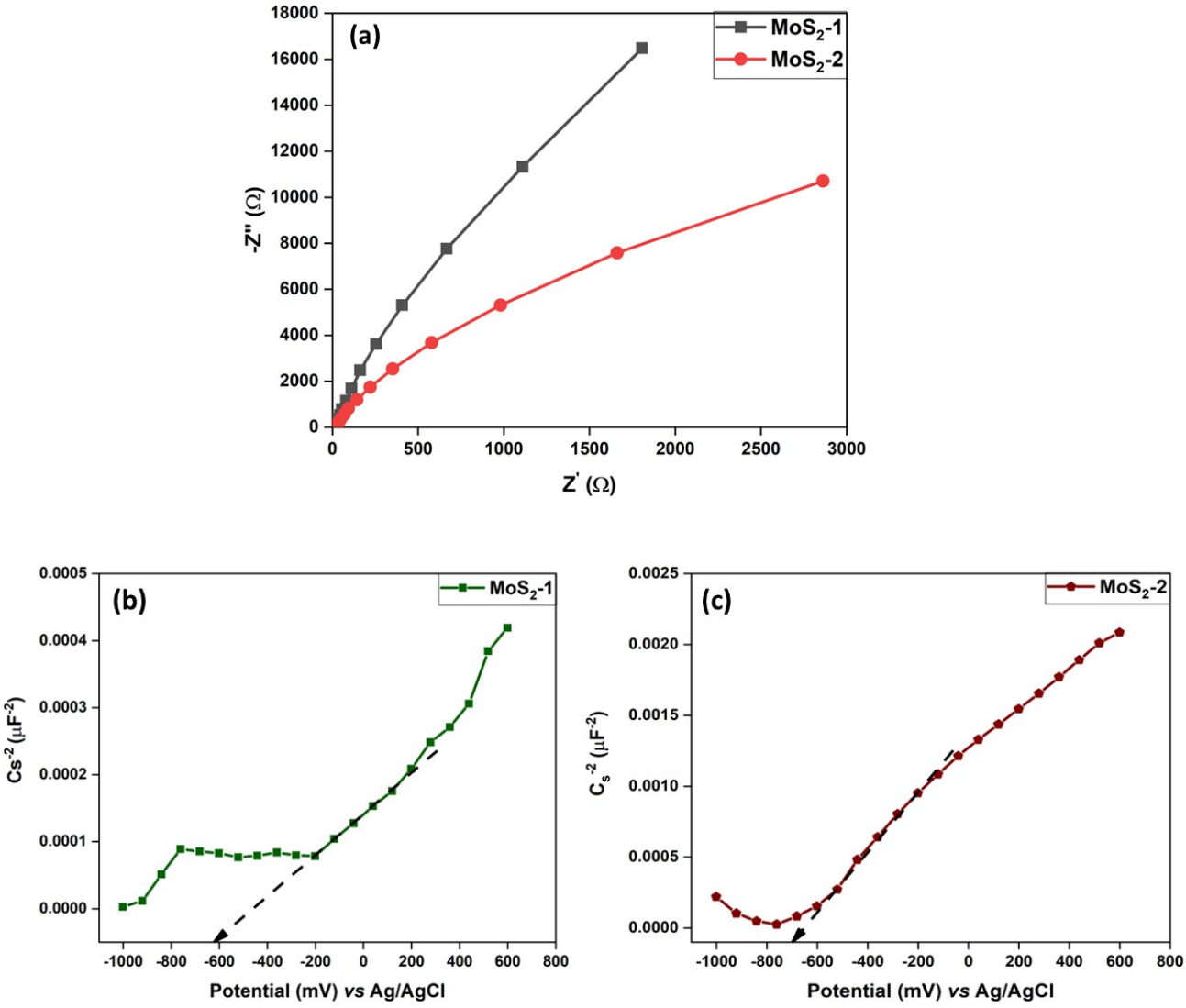

Fig. S7. (a) EIS spectra; (b, c) Mott-Schottky Plots of MoS_2 samples.

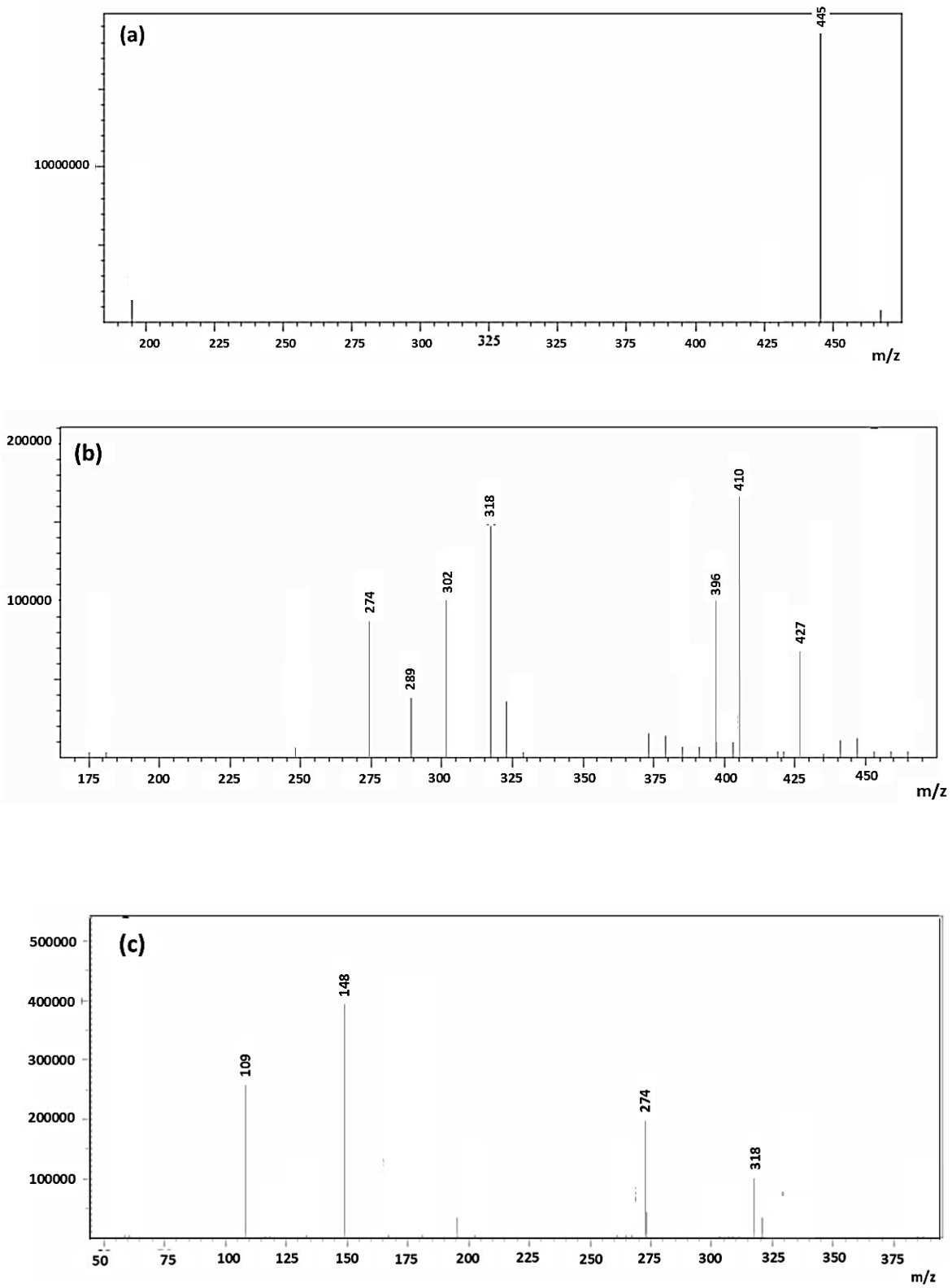

Fig. S8. (a-c) LC-MS/MS Analysis of the TC

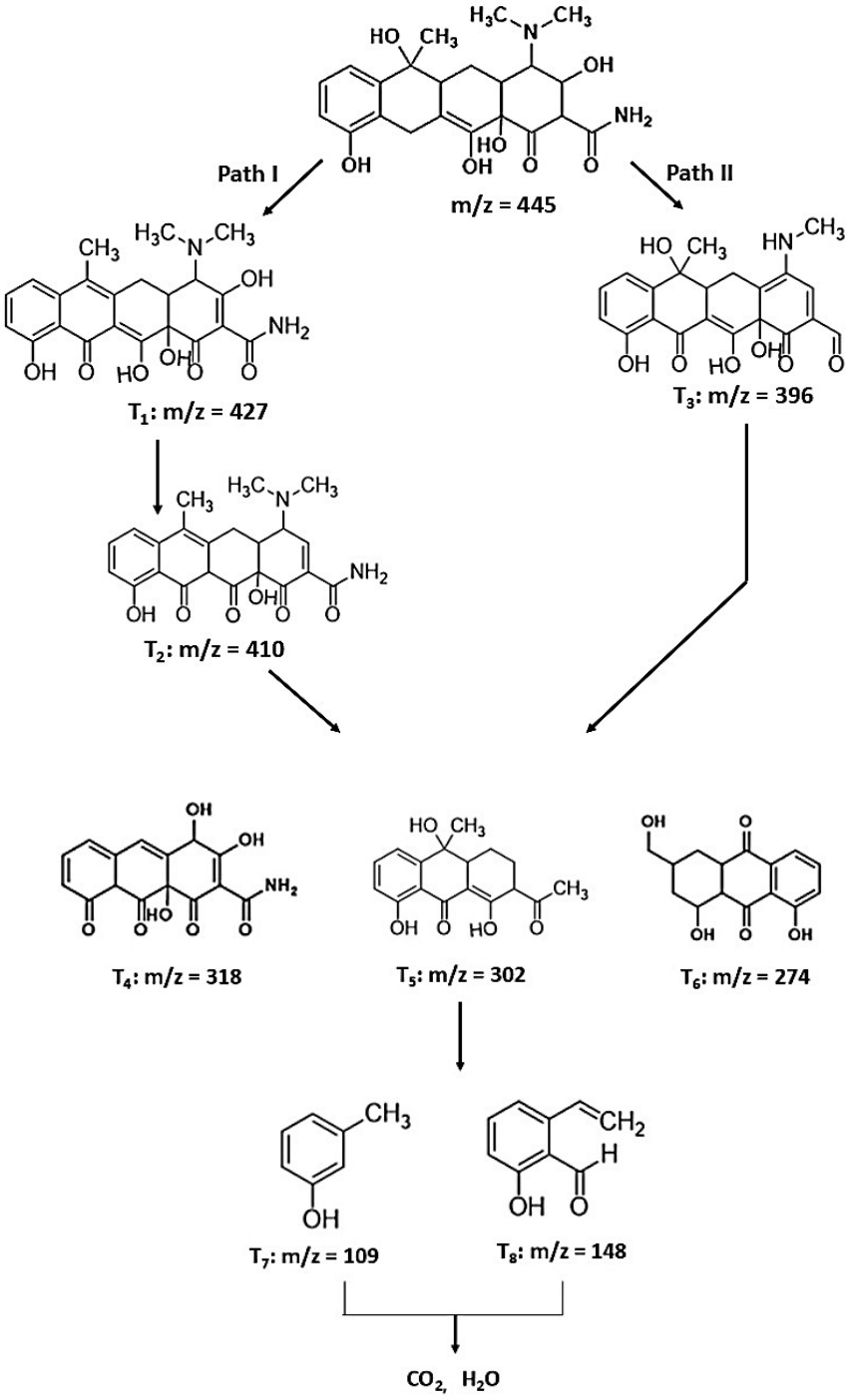

Fig. S9. Degradation pathway of TC.

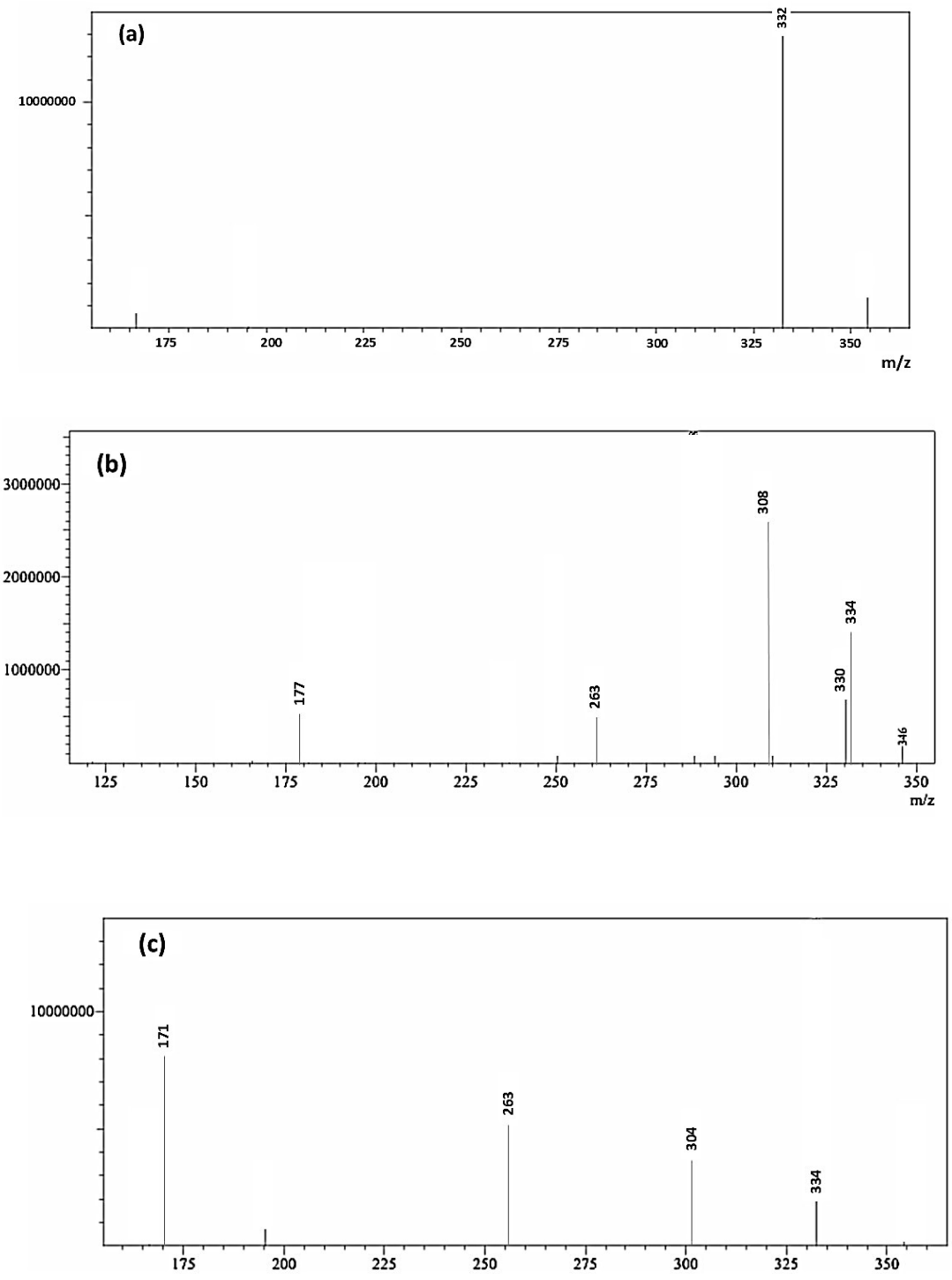

Fig. S10. (a-c) LC-MS/MS Analysis of CIP.

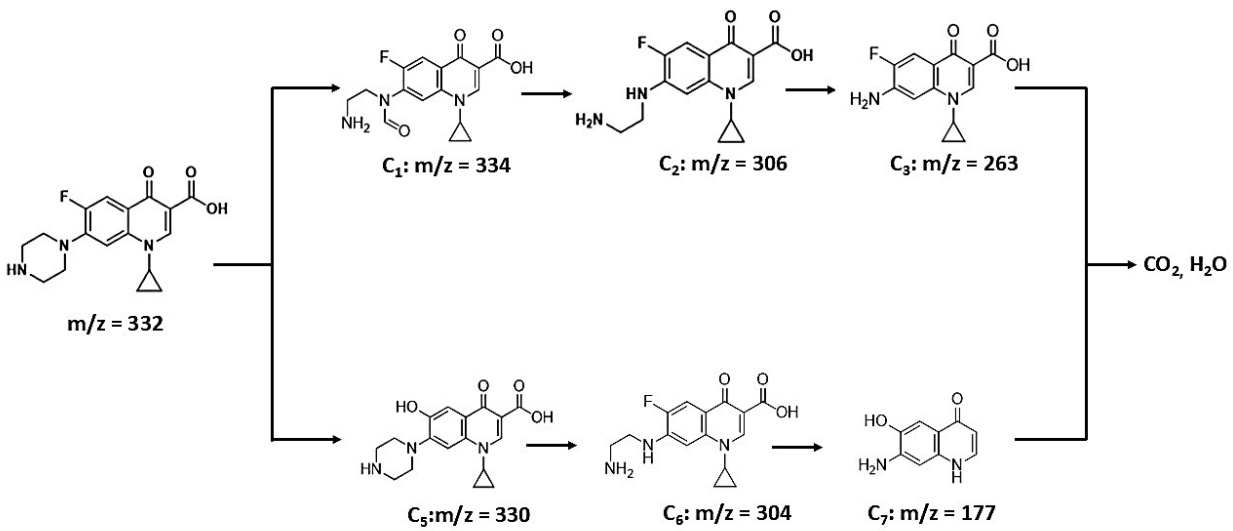

Fig. S11. Degradation pathway of CIP.

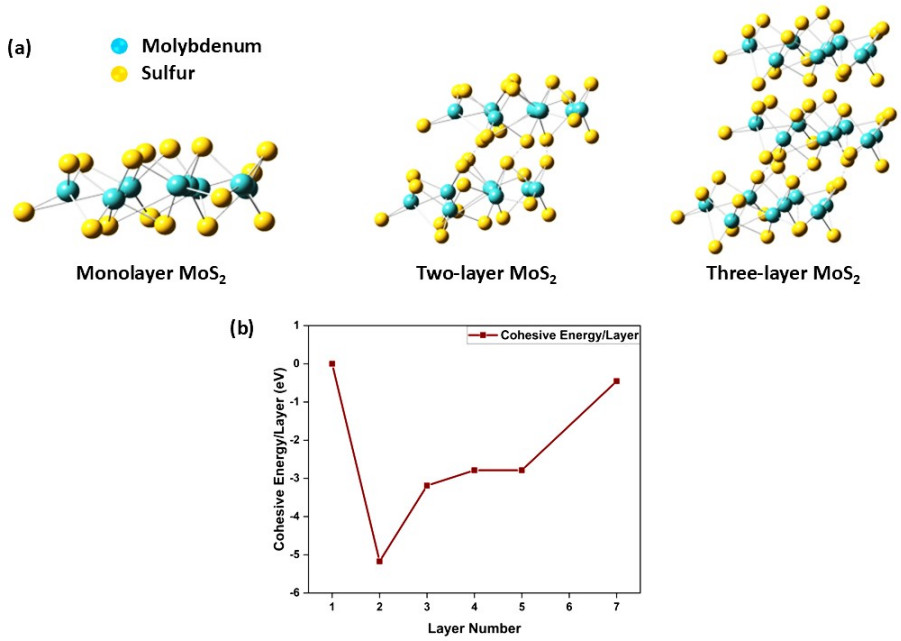

Fig. S12. (a) Optimized DFT structures of 1, 2 and 3-layered MoS_2; (b) Cohesive energy variation with MoS_2 layer numbers.

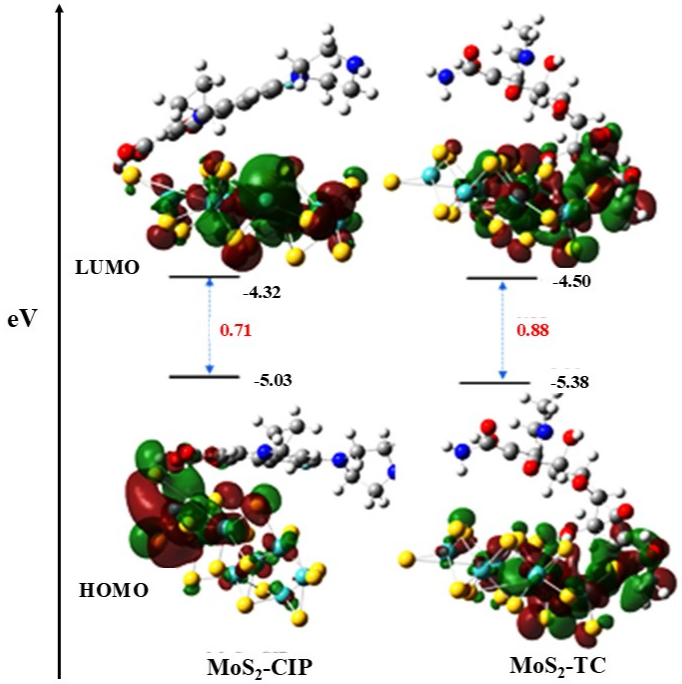

Fig. S13. (a) Frontier molecular orbital (FMO) Analysis of TC–MoS_2 and CIP–MoS_2 complexes showing the corresponding HOMO–LUMO gaps.

References

1. M. J. Frisch, G. W. Trucks, H. B. Schlegel, G. E. Scuseria, M. A. Robb, J. R. Cheeseman, G. Scalmani, V. Barone, G. A. Petersson, and H. Nakatsuji, Gaussian 16 Revision C. 01. 2016, Gaussian Inc., 2016.
2. C. C. Yang, and S. Li. *J. Phys. Chem. C.,* 2009, **113,** 14207-14212.
3. R. Dennington, T. A. Keith, J. M. Millam, GaussView Version 6.1.1, 2019, Semichem Inc. Shawnee Mission KS, 2019
4. T. Lu, and F. Chen, *J. Comput. Chem.,* 2012, **33,** 580–592.
5. W. Humphrey, A. Dalke, and K. Schulten, *J. Mol. Graph.,* 1996, **14,** 33–38.
6. C. P. Prathibha, D. Yashaswini, P. Indhushree, M. R. Lavanya, *RSC Appl. Interfaces,* 2026, **3,** 125-134.
7. V. Salve, P. Agale, S. Balgude, S. Mardikar, S. Dhotre, P. More, *RSC Adv.*, 2025, **15,** 15651-15669.
8. B. R. Anusha, S. Appu, F. Alharethy, G. S. Reddy, M. A. Sangamesha, G. Nagaraju, K. Prashantha, *J. Phys. Chem. Solids.,* 2025, **198,** 112444.
9. T. H. Nguyen, T. D. Cao, T. P. Mai, V. H. Tran, V. T. Pham, V. C. Nguyen, V. T. Nguyen, *RSC Adv.*, 2025, **15,** 25548-25559.
10. I. Altin, R. C. Öztürk, M. Sökmen, I. Altinok, *ChemistrySelect*, 2026, **11,** e05912.
11. L. Chen, C. W. Chen, C. D. Dong, *Chemosphere,* 2025, **370,** 143990.
12. A. Kumar, S. Thakur, R. Kaur, P. Wang, *Surf. Interfaces.,* 2026, **84,** 108546.
13. D. R. Rout, A. Kumar, S. Rtimi, *J. Mater. Chem. A.,* 2025, **13,** 32300-32321.

14. C. Das, T. Shafi, L. P. Thulluru, M. Naushad, B. K. Dubey, S. Chowdhury, *ACS ES&T Water*, 2024, **4,** 2144-2158.
15. C. Das, T. Shafi, B. K. Dubey, S. Chowdhury, *Ind. Eng. Chem. Res.*, 2025, **64,** 7013-7024.
16. O. C. Olatunde, T. L. Yusuf, N. Mabuba, D. C. Onwudiwe, S. Makgato, S. *J. Water Process Eng.,* 2024, **59,** 105074.
17. X. Liu, K. Papadikis, P. S. Yap, G. Dawson, *J. Environ. Chem. Eng.,* 2025, **13,** 119704.
18. C. Fei, Z. Dong, H. Zhou, T. Xu, K. Tang, Y. Fan, R. Mao, *J. Colloid Interface Sci.,* 2025**, 697,** 137920.
19. T. T. Nguyen, J. Singh, V. A. Nguyen, T. L. G. Hoang, P. Nguyen-Tri, *Langmuir*, 2025, **41,** 14229-14243.
20. H. A. Siddiq, A. Alhifthi, R. Ghubayra, M. Madkour, *J. Photochem. Photobiol. A-Chem.,* 2025, **459,** 116073.
21. N. Akhtar, C. Choi, M. Ateeq, P. Fazil, N. S. Shah, J. A. Khan, C. Han, *Chem. Eng. J.,* 2025, **507,** 160336.
22. Q. Chen, C. Liu, R. Liu, Y. Hou, J. Bi, J. C. Yu, L. Wu, *Sep. Purfi. Technol.,* 2025, **355,** 129768.
23. I. Mukherjee, V. Cilamkoti, R. K. Dutta, *ACS Appl. Nano Mater.,* 2021, **4,** 7686-7697.
24. Z. Nasari, M. Taherimehr, *Langmuir,* 2023, **39,** 14357-14373.
25. C. Naga Lakshmi, M. Irfan, N. Singh, *Ind. Eng. Chem. Res.*, 2026, **65,** 1102-1114
26. G. Zuo, H. Ye, J. Du, X. Ding, *J. Nanopart. Res.,* 2025, **27,** 175.